

On-Surface Synthesis and Characterization of Local Magnetic Defects in Kagome Graphene

Rémy Pawlak,^{*,†} Khalid N. Anindya,[‡] Outhmane Chahib,[†] Jung-Ching Liu,[†]
Chao Li,[†] Ali Hamadeh,[¶] Franck Palmino,[¶] Frédéric Chérioux,[¶] Alain
Rocheffort,[‡] and Ernst Meyer^{*,†}

[†]*Department of Physics, University of Basel, Klingelbergstrasse 82, 4056 Basel, Switzerland*

[‡]*Engineering Physics Department, Polytechnique Montréal, Montréal (Québec), H3C 3A7,
Canada*

[¶]*Université de Franche-Comté, FEMTO-ST, CNRS, F-25000 Besançon, France*

E-mail: remy.pawlak@unibas.ch; ernst.meyer@unibas.ch

Abstract

Flat bands in kagome graphene might host strongly electron correlations and frustrated magnetism upon electronic doping. However, the porous nature of kagome graphene opens a semiconducting gap due to quantum confinement, preventing its fine tuning by electrostatic gates. Here we induce zero-modes into a semiconducting kagome graphene by inserting π -radicals at selected locations. We utilize the on-surface reaction of tribromotrioxoazatriangulene molecules to synthesize carbonyl-functionalized kagome graphene on Au(111), thereafter modified *in-situ* by exposure to atomic hydrogen. Atomic force microscopy and tunneling spectroscopy unveil the step-wise chemical transformation of the carbonyl groups into CH radical function, which act as local magnetic defects of spin state 1/2 and leads to zero-energy modes as confirmed by density functional theory. The ability to imprint magnetic defects open up prospects

to study the interplay between topology, magnetism and electron correlation in kagome graphene.

Keywords

Kagome graphene, on-surface synthesis, π -radical, scanning tunneling microscopy, atomic force microscopy, density functional theory

Introduction

Kagome graphene (KG),¹⁻³ a two-dimensional (2D) arrangement of corner-sharing graphene triangles, is long regarded as an ideal candidate for strongly correlated electron phenomena and frustrated magnetism.⁴⁻⁹ Its electronic band structure features van Hove singularities (vHSs), Dirac cones and non-trivial flat bands,⁵ whose filling could be controlled by tuning of the chemical potential using electrostatic gates.^{10,11} Geometrical frustration of kagome lattices might also cause magnetic frustration as exemplary shown in kagome metals,¹²⁻¹⁴ making kagome materials prime candidates for the realization of quantum-spin-liquid states and fractionalized excitations.^{15,16} However, the synthesis of atomically-precise kagome graphene into pure and extended sheets remains a challenging task while its integration into a gate-tunable device has yet to be realized.

On-surface synthesis under ultra-high vacuum (UHV)¹⁷ has become an exciting alternative to fabricate low-dimensional nanographenes with atomic precision,¹⁸⁻²⁰ which structure and electronic properties are investigated at the atomic scale with scanning tunneling microscopy (STM) and atomic force microscopy (AFM).²¹ The rise of carbon-based magnetism in open-shell nanographene²² has further expanded the potential applications of nanographenes to spintronics and quantum technologies, as demonstrated by triangulene derivatives²³⁻²⁷ and few other precursors^{28,29} through the observation of singly occupied/unoccupied molecular orbitals (SOMOs/SUMOs),³⁰ Kondo resonances,²⁴ and spin-flip

excitations using scanning tunneling spectroscopy (STS).^{31,32} In two dimensions, covalent networks with kagome structure were also produced on noble metals using on-surface chemistry,¹⁻³ making them potentially suitable for a transfer into gate-tunable devices.³³ However, their porous character inherently induces large semiconducting gaps due to quantum confinement and heteroatom doping, which shift their flat bands to high energies away from the Fermi level E_F , thus preventing a fine tuning with electrostatic gates. To circumvent this issue, we aim to reproduce the concept introduced by Rizzo *et al.* for semiconducting GNRs³⁴⁻³⁶ consisting in creating zero-mode states through the periodic incorporation of radical sites in the KG structure. Inducing such a low-energy modes might create opportunities to investigate the interplay between topology, magnetism and electron correlation in kagome graphene when directly adsorbed on a metal or in nanoscale devices.

Here, we examine using STM and AFM at low temperature a synthetic strategy to create radical sites in a carbonyl (C=O) functionalized kagome graphene (KG) (Figure 1a). We use the on-surface reactions of tribromotrioxoazatriangulene (BRTANGO) molecules on a Au(111) surface under UHV conditions,^{1,2} in which we replace the peripheral carbonyl groups by CH₂ end groups through their exposure to atomic hydrogen.^{26,30,37} A subsequent thermally-activated dehydrogenation step transforms these groups into C-H radicals embedded into the kagome graphene lattice, as evidenced by a Kondo resonance in tunneling spectra. Despite a low reaction yield of 4-5 %, our results demonstrate a reasonable strategy to engineer local zero-modes in otherwise semiconducting porous nanographene and might serve as a first step for the synthesis of a fully metallic kagome graphene.

Results and Discussion

Electronic structure of the carbonyl-functionalized kagome graphene. BRTANGO molecules were sublimated from a Knudsen cell in UHV on the substrate kept at room temperature (see Methods). AFM image of the isolated precursor and its simulation using the

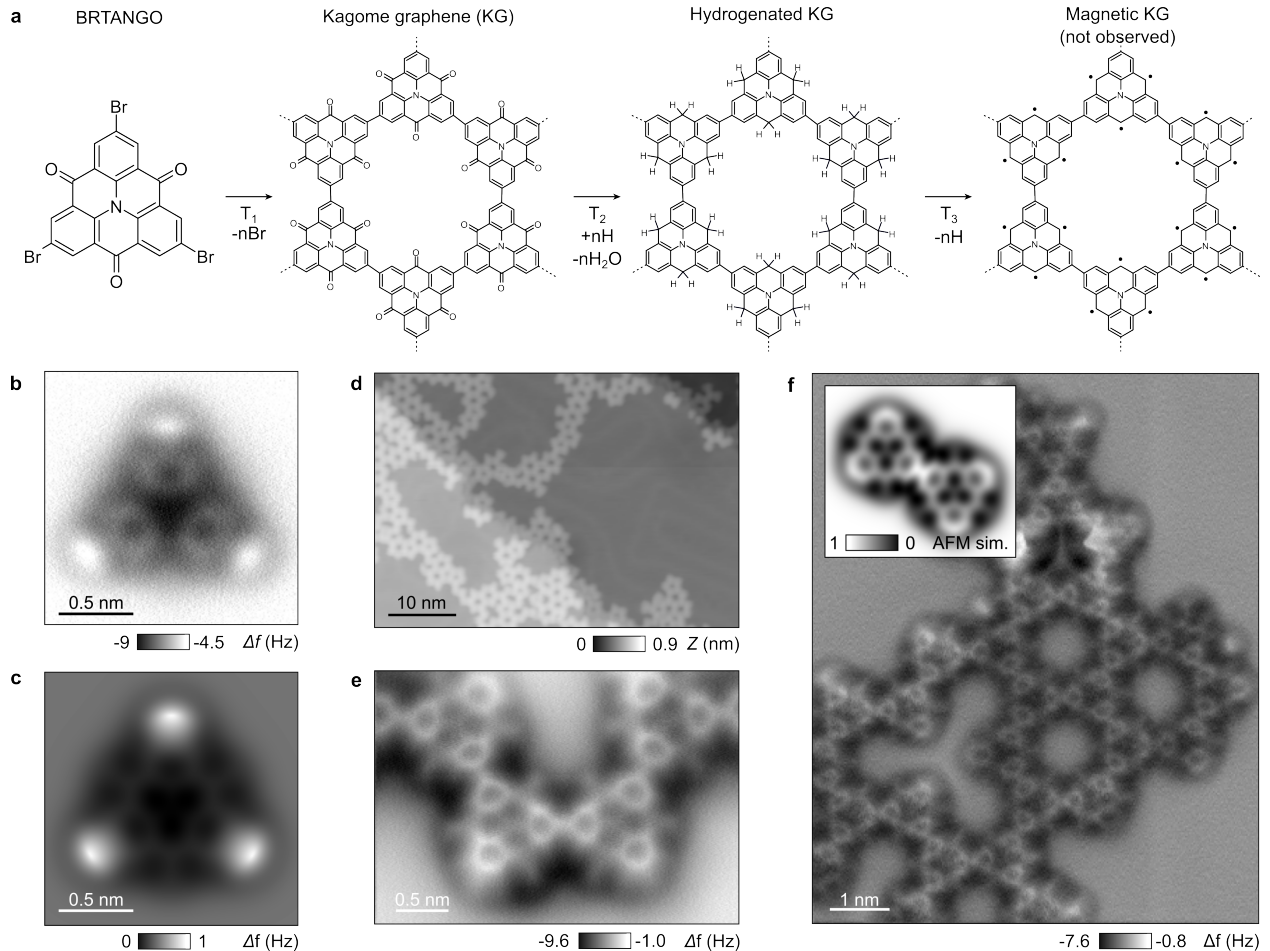


Figure 1: Hierarchical synthesis of local magnetic defects in carbonyl-functionalized kagome graphene. **a**, Chemical structure of the tribromotrioxoazatriangulene (BRTANGO) molecule. **b**, AFM image with a CO-terminated tip of an isolated BRTANGO molecule ($I_t = 1$ pA, $V_s = 0.25$ V) and **c**, Corresponding AFM simulation using the probe-particle model.³⁸ **d**, STM image of the kagome graphene after annealing the substrate at 450 K ($I_t = 1$ pA, $V_s = 0.05$ V). **e-f**, AFM image of the chemical structure of kagome graphene, revealing the covalent coupling between azatriangulene monomers. The inset of **f** shows the simulated AFM image for a covalent dimer.

probe-particle model³⁸ of Figures 1b-c shows the peripheral bromide atoms attached to the corners of the azatriangulene as bright protrusions, while carbonyl side groups appears as dark contrast at edges of the molecule. Annealing the gold substrate to $T_1 = 450$ K initiates the Ullmann coupling reaction (Figure 1a), leading to extended domains of kagome graphene (Figure 1d).^{1,2} Figures 1e and f show representative AFM images of the chemical structure, unveiling the newly formed C-C bounds between azatriangulene monomers. The

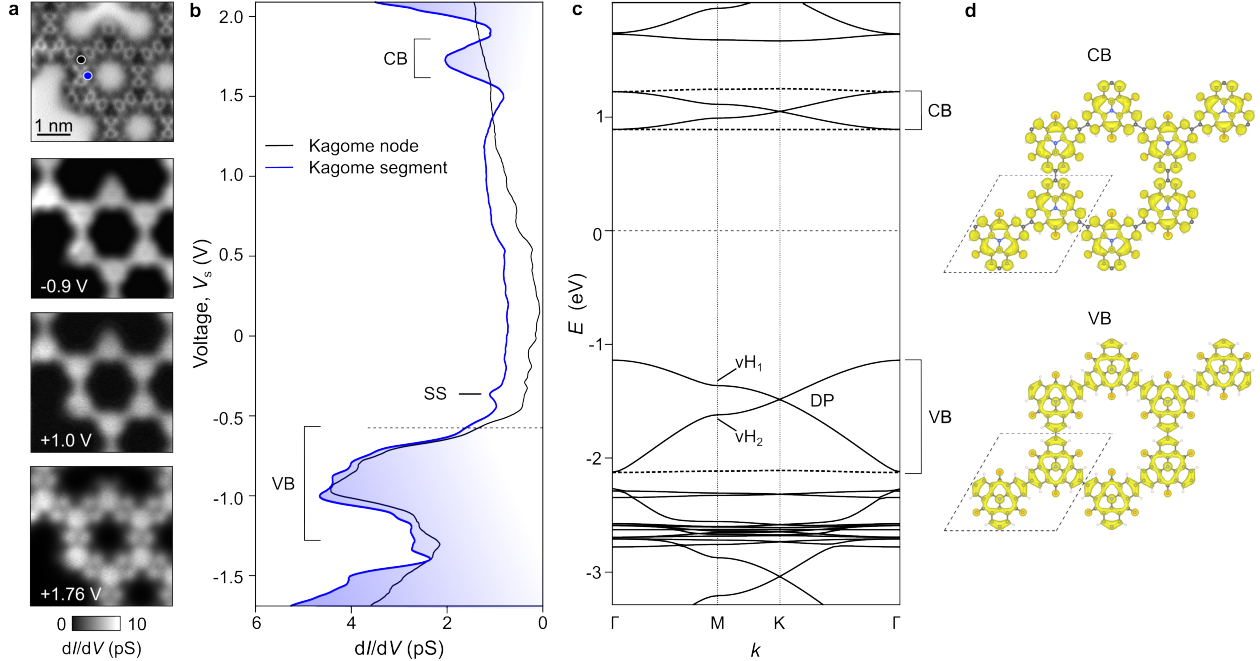


Figure 2: Electronic structure of carbonyl-functionalized kagome graphene. **a**, AFM image of a kagome pore and a series of spatial dI/dV maps recorded at $V_s = -0.9$ V, $+1.0$ V and $+1.76$ V, respectively. **b**, Site-dependent dI/dV spectra acquired at the kagome node (black) and at the kagome segment (blue), ($A_{\text{mod}} = 20$ mV, $f_0 = 611$ Hz). VB and CB correspond to the onset of the valence band (-0.6 eV) and conduction band ($+1$ eV), while SS refers to the confined surface state of Au(111) into the KG pore. **c**, KG band structure calculated by DFT+ U revealing flat conduction bands near 1 eV (dashed line). DP refers to the Dirac point, vH_1 and vH_2 are van Hove singularities. **d**, Frontier orbitals of the KG structure at the CB and VB edges.

AFM contrast also distinguishes carbonyl side groups as faint lines attached to the sides of triangulene. They also appear darker than the intermolecular C-C bonds in relative agreement with the simulated AFM image shown in the inset of Figure 1f. Note finally that, in both the isolated BRTANGO precursor and its polymerized counterpart (Figures 1c and e), the central nitrogen of the molecule always shows a darker contrast than the neighboring carbon atoms.

To gain insight into the KG electronic structure, we acquired site-dependent differential conductance (dI/dV) measurements at 4.4 K (Figure 2). By comparing the spectra acquired at the central nitrogen atom (black dots in Figure 2a) to the segment of the KG lattice (blue), we assign the valence band edge (VB) and conduction band edge (CB) to -0.6 eV

and 1.6 eV, that corresponds to a band gap of about 2.2 eV. This observation confirms the semiconducting character of KG polymer as previously reported in Refs.^{2,6} The resonance at ≈ -450 mV observed at KG segments (blue spectra) is attributed to the confinement of the Au(111) Shockley surface state (SS) by the KG pore. The resonance at +1.75 V is found localized at segments as it vanishes when probing the center of the azatriangulene (black spectra). This is further corroborated by the series of spatial dI/dV maps shown in Figure 2a, revealing the appearance of two lobes at the KG segments for $V_s = 1.76$ V, which disappears for the map at the VB ($V_s = -0.9$ V) or within the gap ($V_s = +1.0$ V).

Using density functional theory (DFT) calculations **with Hubbard U corrections** (see Methods), we calculated the band structure of the free-standing KG (Figure 2c) showing the characteristic features of a kagome graphene : 1- the presence of Dirac cones (DC) and van Hove singularities (vH) due to π -orbitals delocalized across the hexagonal carbon lattice; 2- a series of flat bands (dashed line in Figure 2c) inherited from the kagome geometry. The Dirac points emerge at the K point at about -1.5 eV, -3.1 eV and +1.0 eV, respectively. Three flat bands plotted as blue dashed lines in Figure 2c are positioned at -2.1 eV, 0.9 eV and 1.2 eV, respectively. At about +1 V, the Dirac cone sandwiched by two flat bands is attributed to the broad resonance observed at +1.75 V in the dI/dV spectra of Figure 2b. Similar to the experimental dI/dV map of Figure 2a, the frontier orbitals obtained by DFT+ U (CB of Figure 2d) show an increase of localization of density of states (LDOS) at KG segments and a reduction at the central nitrogen of the azatriangulene. The experimental resonance denoted VB in Figure 2b is attributed to the region including the Dirac cone, a flat band and the two van Hove singularities centered to -1 eV below E_F .

For the sake of completeness, we also investigate the charge distribution of the KG on Au(111) by force spectroscopy (Supporting Figure S2). By measuring the frequency shift Δf as a function of the sample bias V_s at a constant tip-sample separations Z (see Methods),³⁹⁻⁴¹ we probe the electrostatic force acting between tip and sample. As a result, $\Delta f(V)$ curves present a parabolic shape, in which the voltage corresponding to the top of the

parabola (noted V^*) represents the local contact potential difference (LCPD) between tip and sample. Thus, the local variation of LCPD between site-dependent $\Delta f(V)$ curves allows us to estimate the charge distribution and local changes of work function down to the sub-molecular scale.^{39–41} Supporting Figure S2b shows a $\Delta f(V)$ cross-section acquired along two azatriangulene monomers (white line in the AFM image of Supporting Figure S2a). Single $\Delta f(V)$ point-spectra acquired on top of Au(111) (red), at the central N atom (black) and between the monomers (blue) are plotted in Supporting Figure S2c, respectively. Dashed lines mark the LCPD value (V^*) for each position. The LCPD value systematically shifts towards more positive values ($\Delta V^* \approx 0.15$ and 0.23 V) for the KG structure as compared to the pristine Au substrate, with a maximum value of 0.23 V for the central N atom of the azatriangulene. This indicates an accumulation of negative charges at the KG structure as compared to the Au substrate, which we attribute to a charge transfer from the substrate to the KG polymer due to its accepting character.³⁰

Hydrogenation of the carbonyl groups. To hydrogenate peripheral C=O groups, we exposed the kagome graphene on Au(111) held at room temperature in UHV to atomic hydrogen (see Methods).^{26,30} This substitution reaction transforms carbonyl sides groups of azatriangulene monomers into sp^3 -hybridized carbon atoms (CH_2 groups) as depicted in Figure 1a. This turns substituted azatriangulene monomers three-dimensional due to the formation of bulky CH_2 side groups at their sides.³⁰ Supporting Figures 1a and b show high-resolution STM/AFM images of the KG lattice after such preparation. While in STM topographic image the formed CH_2 groups can be difficult to identify, they become more apparent by AFM imaging as its contrast is more sensitive to three-dimensional relaxations of molecules (see yellow arrows). Supporting Figure 2c also shows close-up AFM images of a monomer with a single CH_2 side group, along with a bond-resolved STM (BRSTM) image. To estimate the yield of the substitution reaction of azatriangulene monomers, we systematically characterized large areas of the KG/Au(111) samples using AFM imaging.

While each monomer contain three carbonyl groups, we only observed the substitution of one carbonyl per molecules. Although numerous preparation procedures have been explored (in which we varied the H_2 exposure time, the sample temperature and the number of cycles), we did not reach a reaction yield superior than 11-15 %. Considering that each molecule has three carbonyls, the yield turning carbonyls into CH_2 groups is thus not exceeding 4-5 %. We think that the KG might decrease the diffusion of atomic hydrogen on the surface and limits the reaction yield. Also, the covalent character of the 2D KG polymer can prevent its geometric relaxation upon reaction, which may drastically reduce the hydrogenation reaction.

Kondo resonance and zero-mode of π -radicals. The synthesis of π -radicals is obtained by annealing the substrate to $T_3 = 300$ °C leading to the partial dehydrogenation of the CH_2 side groups into CH function (Figure 1a).³⁰ Figures 3a and b show representative STM and AFM images of the KG structure after such treatment. At low bias value ($V_s \approx 15$ mV), STM images reveal bright features superimposed to a few monomers as exemplarily shown with a yellow arrow in Fig. 3a. As compared to the hydrogenated KG (Supporting Figure S2), the AFM image now shows only planar monomers, even for those with bright STM contrasts. The absence of any geometrical relaxations of monomers thus indicates the successful dehydrogenation of the CH_2 side groups and the presence of radical CH sites. This observation is further corroborated by the zero-energy dI/dV map of Figure 3c, that reflects the spatial signature of the zero-energy states. Similar for all the reacted monomers, this spatial signature is analogous to that of Kondo resonances for π -electrons in nanographene.^{26,30}

We next characterize by AFM the KG chemical structure after the dehydrogenation reaction. Figures 3d-f presents an AFM close-up where two of the monomers exhibit zero-energy modes. The radical CH groups appear in the AFM image as a bright line at one side of the monomer (pointed by a yellow arrow in Figure 3d), which is opposed to the dark contrast of carbonyl groups (orange arrow). By assuming the observed chemical structure in gas-phase with two radical sites (Figure 3e), we simulated the AFM image using the

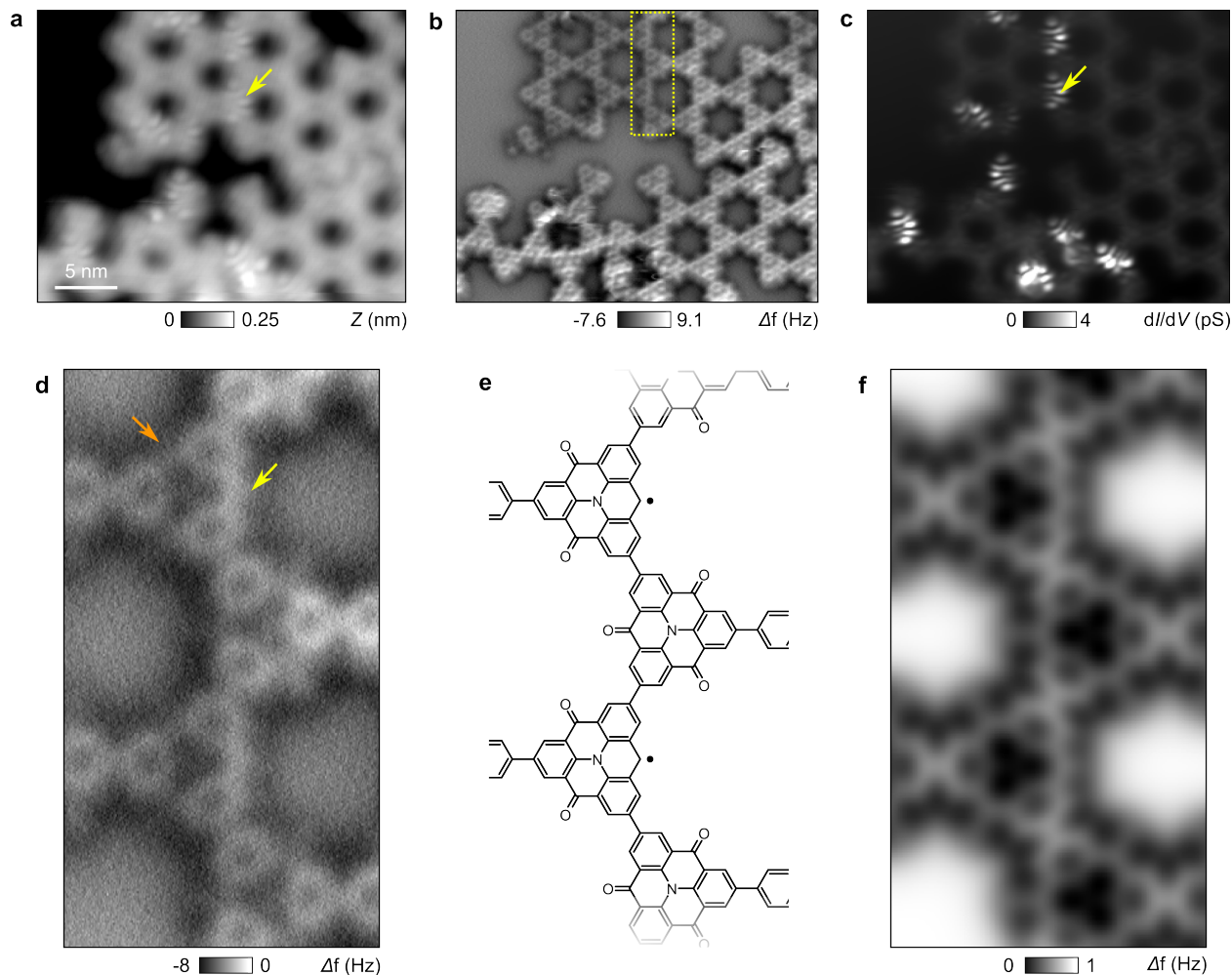


Figure 3: Structural characterization of radical sites by STM/AFM. **a**, STM overview image of the KG after dehydrogenation of CH_2 groups ($I_t = 1$ pA, $V_s = 0.05$ V) and **b**, Corresponding AFM image with a CO-terminated tip ($f_0 = 26$ kHz, $A_{\text{osc}} = 50$ pm). **c**, Spatial dI/dV maps acquired at zero-energy. Bright features (yellow arrows) corresponds to the zero-energy modes arising from the presence of π -radicals of the KG. **d**, Close-up AFM image distinguishing carbonyl side groups (orange arrow) and π -radicals (yellow arrow). **e**, Deduced chemical structure in gas-phase and **f**, the simulated AFM image.

probe-particle model shown in Figure 3f. The excellent agreement between simulation and experiment thus allows us to correlate these zero-energy modes to the presence of π -radical side groups in the KG structure.

To characterize the magnetic signature of radical sites, we performed low-energy dI/dV point-spectra at $T = 4.5$ K. Figure 4a shows the STM topographic image and an AFM image of a reacted monomer together with its zero-energy dI/dV map. The yellow arrow points

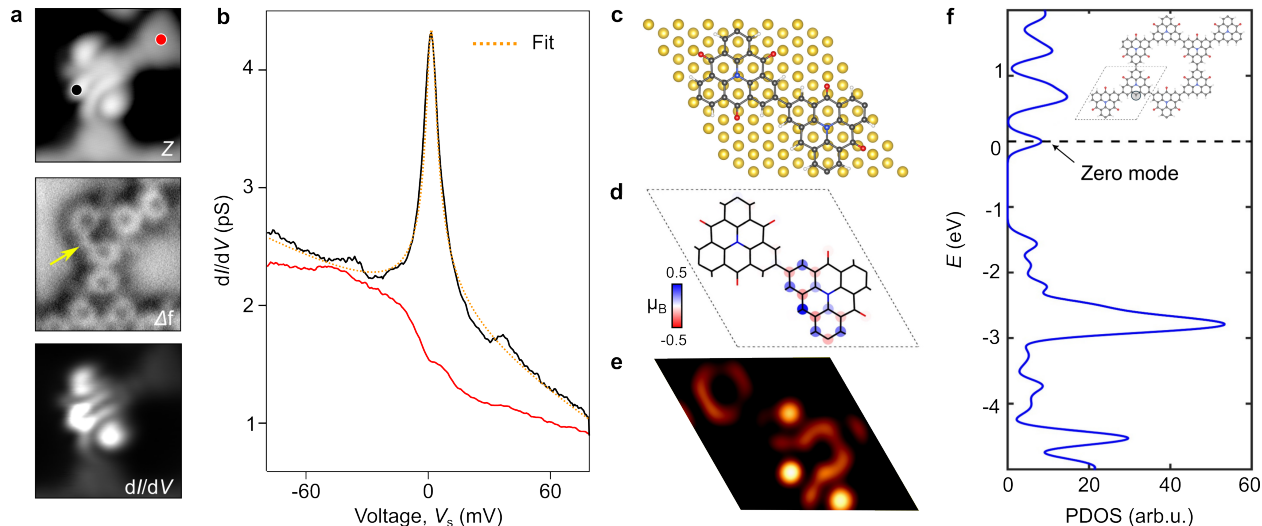


Figure 4: Kondo resonance of the radical groups. **a**, STM topography, AFM image and zero-energy dI/dV map of a reacted monomer. **b**, Low-energy dI/dV spectra acquired at the black and red dots in **a** corresponding to a reacted (black) and an unreacted monomer (red), respectively. Lock-in amplitude: 1.5 mV, $f_0 = 611$ Hz. A Hurwitz-Fano lineshape⁴² is used to fit the zero-bias peak, which we attribute to a Kondo resonance from the spin-1/2 π -radical with a Kondo temperature T_K of ≈ 21 K. **c**, Structure of a dimer on Au with one radical sites and **d**, the spin density. **e**, Simulation of the STM image using the Tersoff-Hamman approximation. **f**, Density of states (DOS) calculated by DFT+ U showing the zero-mode induced by a radical in the KG (black dots in the inset).

to the position of the radical site. In Figure 4b, we plot representative dI/dV point-spectra recorded at the radical (black) as compared to a pristine molecule (red), which positions are shown in Fig. 4a. The sharp zero-bias peak observed at the radical site, absent for the unreacted monomer, is attributed to a Kondo resonance from the spin 1/2 state of the CH radical.²⁴ Its linewidth (FWHM ≤ 7.2 mV) extracted from fitting few experimental spectra with the Hurwitz-Fano lineshape⁴² is consistent with a Kondo temperature of ≈ 21 -25 K.

We further explored the electronic structure of a radical site in KG using DFT+ U . The relaxed structure of the unit-cell (UC) we considered is shown in Fig. 4c, which includes a covalent dimer with one radical adsorbed on Au(111) substrate, aligning well with the experimental structure. The calculated non-spin-polarized density of states (DOS) for free-standing KG lattice with one radical (black transparent circle in the inset of Fig. 4f) shows appearance of a non-bonding zero-mode state at the Fermi level, indicating a high-spin state

in this 2D-KG lattice. Additionally, we observed the opening of a Coulomb gap in the spin-polarized DOS (Supporting Figure S3), representing the ground state of the system. This gap results from the repulsive energy cost associated with unpaired spins attempting to occupy the same site in this magnetic system.⁴³ Furthermore, our theoretical spin-density map (see Fig. 4d) of the one radical per UC system supports the experimental zero-energy dI/dV map, showing magnetic moments along the defect site but no magnetism at the no-defect site of the UC. This aligns well with our calculated LDOS map showing the localized nature of the unpaired electron (see Fig. 4e) which also matches with the experimental constant-height dI/dV maps obtained at zero-energy (Figure 4), validating our theoretical approach to study this system. Using a 2x2 supercell, we have estimated the Heisenberg spin exchange parameter,⁴⁴ $J = E_{\text{AF}} - E_{\text{FM (triplet)}} \approx 0$ meV for this 2D-KG lattice with one radical per UC, indicating its paramagnetic nature.

Building on our experimental findings, we extended our investigation into the influence of multiple defects per unit cell (UC) for the 2D-KG system. Starting with two and four defects per UC, as shown in Supporting Figures S4b-c respectively, we observed clear antiferromagnetic (AF) coupling between the spin sites of neighboring monomers forming the UC (see Figures S4f-g). The energy differences between the AF ground state and the ferromagnetic (FM) state are indicated at the bottom of each figure, highlighting the system’s energetic preferences. Interestingly, in the case of four defects per UC, the system displayed FM coupling between the spin sites within a monomer, while maintaining a collective AF coupling between neighboring monomers. This magnetic behaviour mirrors that of the triangulene dimer system, which also features four unpaired electrons and exhibits similar magnetic properties.⁴³

Turning to panels d and h of Supporting Figures S4, where the system includes six free radicals per UC, we observe an unexpected deviation in spin configuration. Despite the expectation that each monomer would exhibit a spin state of $S = 3/2$ based on the number of free radicals, the Jahn–Teller distortion reduces the spin state to $S = 1/2$ for each

monomer.²⁶ This distortion lifts the degeneracy of the electronic configuration, stabilizing the system by lowering its overall energy. Within individual monomer, AF coupling occurs between adjacent atoms, ensuring that the system adheres to Ovchinnikov’s rule,⁴⁵ which requires alternating spin states between adjacent atoms in organic conjugated systems. However, the small energy difference of 4.5 meV between the AF and FM states in Supporting Figures S4h suggests a very subtle preference for the FM configuration between monomers, although the system would remain paramagnetic at certain temperatures or external conditions. This intricate balance between FM and AF interactions in the presence of multiple defects per UC underscores the significant role played by structural distortions, such as the Jahn–Teller effect, in modulating the system’s magnetic properties. Despite the presence of six free radicals and the potential for higher spin states, the reduction to $S = 1/2$ and the maintenance of AF coupling between neighboring atoms within monomers demonstrate the robustness of Ovchinnikov’s rule.

Figure 5 presents the band structures for the 2D-KG system, focusing on configurations with 1, 2, 4, and 6 defects per UC, all in their ferromagnetic (FM) states. Although the 2- and 4-defect systems have antiferromagnetic (AF) ground states, we focus on their FM states for a more consistent comparison. As the number of defects increases, the figure highlights how defect concentration influences the spin polarization, symmetry breaking, and the overall electronic structure, particularly the disruption and eventual recovery of Dirac cones for 6 defects case with high symmetry.

In the case of the system with 1 defect per UC (see Figure 5a), the band structure shows distinct spin-up (blue) and spin-down (red) channels, indicating clear spin polarization caused by the paramagnetic ordering. The introduction of a single defect disrupts the symmetry of the pristine Kagome lattice, which is most notably seen at the K-point in the Brillouin zone (BZ), where the characteristic Dirac cones are broken. Despite this symmetry breaking, the bands still show some dispersion, particularly around the Fermi level, indicating that while there is some localization, the system retains a level of electronic mobility.

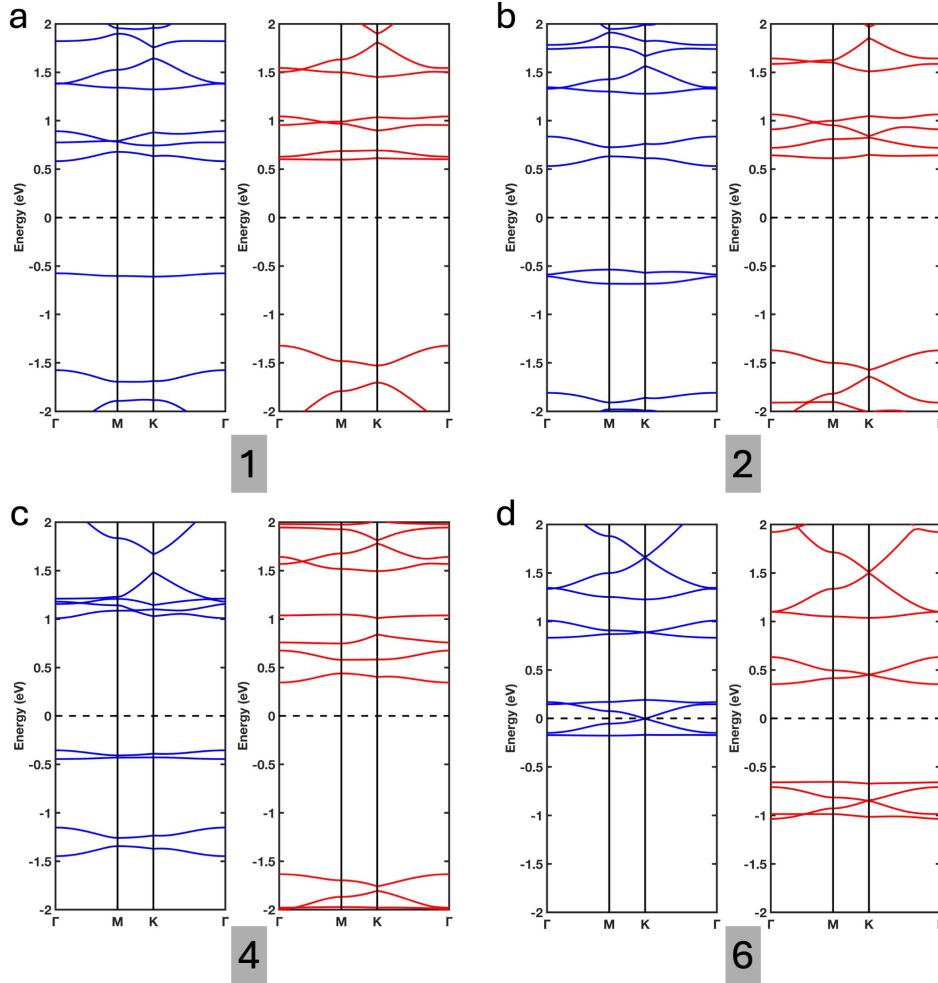


Figure 5: Band structures of the 2D-KG system with 1, 2, 4, and 6 defects per unit cell (**a-d**) in their ferromagnetic (FM) states, showing α (blue) and β (red) spin channels. The number of defects is indicated in the gray-shaded box on each panel. The figure highlights the impact of defect concentration on spin polarization, symmetry breaking, and the disruption and reformation of Dirac cones.

The moderate splitting of the spin channels, along with the remaining dispersive bands, suggests that the 1-defect configuration only weakly localizes the electronic states, maintaining a relatively conductive behaviour.

Interestingly, with 2 defects per UC (see Figure 5b), we see less disruption in the Dirac cone compared to the 1-defect system. Although there are more defects in this configuration, the interaction between the two defects within the UC introduces some symmetry compensation. The two defects are arranged in such a way that their combined effect on the lattice

periodicity is more balanced than in the 1-defect case. This results in a more subtle disruption of the Dirac cones at the K-point, and the bands near the Fermi level remain slightly more dispersive, indicating reduced localization. In contrast, with 4 defects per UC, the band structure shows pronounced localization as shown in Figure 5c. The bands around the Fermi level are extremely flat, reflecting strong localization of electronic states. The breaking of Dirac cones is severe, pointing out a significant reduction in the symmetry of the system. The flattening of bands near the Fermi level implies that the electronic states are strongly confined, and the system's electronic properties are dominated by defect interactions and symmetry breaking.

However, the system with 6 defects per UC shows a different behaviour from the other configurations. Despite the high defect concentration, the symmetry of the system is regained, leading to the reformation of Dirac cones at the K-point (see Figure 5d). This recovery of symmetry results in a return to more dispersive bands near the Fermi level, which are characteristic of Dirac-like systems with higher electronic mobility. The reappearance of Dirac cones in the 6-defect configuration suggests that the lattice undergoes a reordering that restores periodicity, even in the presence of numerous defects. This symmetry restoration is a remarkable departure from the trend of increasing localization seen in the 2- and 4-defect systems. Although the Jahn–Teller distortion reduces the expected spin state of each monomer from $S = 3/2$ to $S = 1/2$ in this 6-defects systems, this structural distortion does not prevent the overall system from regaining its symmetry. This behaviour indicates that the 6-defect system not only recovers its electronic symmetry but also exhibits high-mobility electronic states, contrasting sharply with the highly localized behaviour observed in the 4-defect system.

Conclusion

In summary, we have investigated by means of high-resolution AFM a synthetic route to produce radical sites in a carbonyl-functionalized kagome graphene and demonstrated their magnetic signature by tunneling microscopy. The synthesis of kagome graphene was obtained by an on-surface reaction of tribromotrioxoazatriangulene (BRTANGO) molecules on an Au(111) substrate. We next exposed the KG/Au(111) sample to atomic hydrogen in UHV in order to substitute the carbonyl (C=O) groups of azatriangulene monomers by CH₂ functions. A subsequent annealing dehydrogenate these CH₂ groups leading to CH radical sites attached at the monomer side as confirmed by AFM imaging. Using tunneling spectroscopy at low temperature, we demonstrated the magnetic state of the radicals by detecting a Kondo resonance. Combining experimental dI/dV maps and DFT+ U calculations, we show that the radicals have a $S = 1/2$ spin state which is accompanied by the introduction of low-energy modes in the band structure of the semiconducting kagome graphene. Our synthetic approach might enable the experimental realization of a metallic kagome graphene, which would allow the study of the interplay between topology, magnetism and electron correlation in kagome graphene systems. **Additionally, our study of the 2D-KG system with varying defect concentrations revealed how defects influence symmetry, magnetism, and electronic localization. Notably, increasing defects led to greater localization and symmetry disruption, except in the 6-defects system where symmetry and Dirac cones were unexpectedly restored, enhancing electronic mobility. This demonstrates the potential of defect engineering to tune the electronic and magnetic properties of 2D materials for spintronics and quantum devices.**

Supporting Information

The Supporting Information is available free of charge at !!!

Methods

Sample preparation. The Au(111) substrate purchased from Mateck GmbH was sputtered by Ar^+ ions and annealed at 550 °C to remove any surface contaminations. BRTANGO precursors were synthesized following the procedure described here.³⁰ Molecules were sublimed from a Knudsen cell kept at 240 °C in UHV. During sublimation, the sample was kept at about 200°C to promote the formation of well-extended Kagome graphene domains. For the hydrogenation of the sample, we reproduced the preparation procedure from reference.³⁰ We used a atomic hydrogen source purchased from Focus GmbH with a leak valve connected to the preparation chamber. After filling the chamber with a H_2 pressure of 2×10^{-7} mbar, we heated the tungsten filament to 2500 °C until an emission power of 80 W was reached. The sample was then placed in front of the source for 4 minutes by opening the source shutter.

STM experiments. The STM experiments were conducted at a temperature of 4.8 K using an Omicron GmbH low-temperature STM/AFM system operated with Nanonis RC5 electronics. Differential conductance spectroscopy $dI/dV(V)$ spectra were acquired with the lock-in amplifier technique using a modulation of 610 Hz and a modulation amplitude of 10 meV. All voltages refer to the sample bias V_s with respect to the tip.

AFM experiments. AFM measurements were performed with commercially available tuning-fork sensors in the qPlus configuration⁴⁶ equipped with a tungsten tip ($f_0 = 26$ kHz, $Q = 8000$ to 25 000, nominal spring constant $k = 1800$, N.m^{-1} , oscillation amplitude $A \approx 50$ pm. Constant-height AFM images were obtained using tips terminated with a single carbon monoxide (CO) in the non-contact mode (frequency-modulated AFM–FMAFM) at zero voltage.^{21,47} CO molecules were adsorbed on the sample maintained at low temperature below 20 K. Before its functionalization, the apex was sharpened by gentle indentations into the gold surface. A single CO molecule was carefully attached to the tip following the

procedure of reference.⁴⁸ Simulations of the AFM images based on the DFT coordinates were carried out using the probe-particle model.³⁸ The $\Delta f(V)$ cross-section of 1×40 pixels² was acquired with Au-coated metallic tips (tunneling setpoints: $I_t = 1$ pA, $V_s = 200$ mV, $Z_{\text{offset}} = -50$ pm).

DFT calculations. To investigate the electronic and magnetic properties of the 2D-KG with different number of defects, we employed the density functional theory (DFT) with the Hubbard correction (DFT+ U) as implemented in the Quantum ESPRESSO package.^{49,50} This approach is necessary to account for the localized spin contributions and strong electron correlation effects within the 2D-KG lattice. We utilized the Perdew-Burke-Ernzerhof (PBE) functional⁵¹ in our DFT+ U approach, which has been validated in our prior studies to yield accurate results for similar 2D systems.^{8,52} The Hubbard U parameter for the C 2p orbitals was derived using the linear response method,⁵³ ensuring a consistent treatment of on-site electron-electron interactions. For the geometry optimization of the TANGO 2D Kagome lattice, we employed an energy convergence threshold of 10^{-6} Ry and a force convergence criterion of 10^{-4} Ry/Å. A plane-wave cutoff energy of 50 Ry was used, and the Brillouin zone was sampled using a Monkhorst-Pack k-point grid of $6 \times 6 \times 1$ for the unit cell optimization. For electronic structure and magnetic properties calculations, a denser k-point mesh of $12 \times 12 \times 1$ was employed. A vacuum region of 20 Å was applied along the z-direction to avoid spurious interactions between periodic images, ensuring accurate representation of the 2D nature of the system. Spin-polarized calculations were performed to explore both antiferromagnetic (AF) and ferromagnetic (FM) coupling scenarios within the TANGO lattice, with spin alignments restricted along the z-axis for computational efficiency. The total magnetic moments and spin-density distribution were analyzed to explore the Jahn-Teller effects and magnetic couplings in the presence of multiple defects per unit cell (UC), as discussed in the main text. In addition to DFT+ U , van der Waals (vdW) interactions were included using Grimme’s D2 method⁵⁴ to capture weak interlayer interactions where

applicable. Projector-augmented wave (PAW) pseudopotentials were used to describe the interaction between ions and valence electrons,^{55,56} ensuring accuracy in both the structural and electronic properties.

Acknowledgement

E.M. and R.P. acknowledge funding from the Swiss Nanoscience Institute (SNI), the European Research Council (ERC) under the European Union’s Horizon 2020 research and innovation programme (ULTRADISS grant agreement No 834402 and supports as a part of NCCR SPIN, a National Centre of Competence (or Excellence) in Research, funded by the SNF (grant number 51NF40-180604). E.M., R.P. and T.G. acknowledge the Sinergia Project funded by the SNF (CRSII5_213533) and the SNF grant (200021_228403). K.N.A. thanks the Fonds de recherche du Québec (FRQ) for scholarship through the PBEEE merit scholarship program. T.G. acknowledges the FET-Open program (Q-AFM grant agreement No 828966) of the European Commission. J.-C.L. acknowledges funding from the European Union’s Horizon 2020 research and innovation programme under the Marie Skłodowska-Curie grant agreement number 847471. A.R. and K.N.A. acknowledges the support from the Natural Sciences and Engineering Research Council of Canada (NSERC), and they are grateful to Calcul Québec and the Digital Research Alliance of Canada (The Alliance) for providing the computational resources.

References

- (1) Steiner, C.; Gebhardt, J.; Ammon, M.; Yang, Z.; Heidenreich, A.; Hammer, N.; Görling, A.; Kivala, M.; Maier, S. Hierarchical on-surface synthesis and electronic structure of carbonyl-functionalized one- and two-dimensional covalent nanoarchitectures. *Nat. Comm.* **2017**, *8*, 14765.

- (2) Galeotti, G. et al. Synthesis of mesoscale ordered two-dimensional π -conjugated polymers with semiconducting properties. *Nat. Mater.* **2020**, *19*, 874–880.
- (3) Pawlak, R.; Liu, X.; Ninova, S.; D’Astolfo, P.; Drechsel, C.; Liu, J.-C.; Häner, R.; Decurtins, S.; Aschauer, U.; Liu, S.-X.; et al, On-Surface Synthesis of Nitrogen-Doped Kagome Graphene. *Angew. Chem. Int. Ed.* **2021**, *60*, 8370–8375.
- (4) Wang, Z. F.; Su, N.; Liu, F. Prediction of a Two-Dimensional Organic Topological Insulator. *Nano Lett.* **2013**, *13*, 2842–2845.
- (5) Chen, Y.; Xu, S.; Xie, Y.; Zhong, C.; Wu, C.; Zhang, S. B. Ferromagnetism and Wigner crystallization in kagome graphene and related structures. *Phys. Rev. B* **2018**, *98*, 035135.
- (6) Jing, Y.; Heine, T. Two-Dimensional Kagome Lattices Made of Hetero Triangulenes Are Dirac Semimetals or Single-Band Semiconductors. *Jour. Amer. Chem. Soc.* **2019**, *141*, 743–747.
- (7) Neupert, T.; Denner, M. M.; Yin, J.-X.; Thomale, R.; Hasan, M. Z. Charge order and superconductivity in kagome materials. *Nat. Phys.* **2022**, *18*, 137–143.
- (8) Anindya, K. N.; Rochefort, A. Controlling The Magnetic Properties of Two-Dimensional Carbon-Based Kagome Polymers. *Carbon Trends* **2022**, *7*, 100170.
- (9) Catarina, G.; Henriques, J. C. G.; Molina-Sánchez, A.; Costa, A. T.; Fernández-Rossier, J. Broken-symmetry magnetic phases in two-dimensional triangulene crystals. *Phys. Rev. Res.* **2023**, *5*, 043226.
- (10) Chen, G.; Sharpe, A. L.; Fox, E. J.; Zhang, Y.-H.; Wang, S.; Jiang, L.; Lyu, B.; Li, H.; Watanabe, K.; Taniguchi, T.; Shi, Z.; Senthil, T.; Goldhaber-Gordon, D.; Zhang, Y.; Wang, F. Tunable correlated Chern insulator and ferromagnetism in a moiré superlattice. *Nature* **2020**, *579*, 56–61.

- (11) Choi, Y.; Kim, H.; Peng, Y.; Thomson, A.; Lewandowski, C.; Polski, R.; Zhang, Y.; Arora, H. S.; Watanabe, K.; Taniguchi, T.; Alicea, J.; Nadj-Perge, S. Correlation-driven topological phases in magic-angle twisted bilayer graphene. *Nature* **2021**, *589*, 536–541.
- (12) Balents, L. Spin liquids in frustrated magnets. *Nature* **2010**, *464*, 199–208.
- (13) Ye, L.; Kang, M.; Liu, J.; von Cube, F.; Wicker, C. R.; Suzuki, T.; Jozwiak, C.; Bostwick, A.; Rotenberg, E.; Bell, D. C.; Fu, L.; Comin, R.; Checkelsky, J. G. Massive Dirac fermions in a ferromagnetic kagome metal. *Nature* **2018**, *555*, 638–642.
- (14) Kumar, D.; Hellerstedt, J.; Field, B.; Lowe, B.; Yin, Y.; Medhekar, N. V.; Schiffrin, A. Manifestation of Strongly Correlated Electrons in a 2D Kagome Metal–Organic Framework. *Adv. Func. Mater.* **2021**, *31*, 2106474.
- (15) Harris, A. B.; Kallin, C.; Berlinsky, A. J. Possible Néel orderings of the Kagomé anti-ferromagnet. *Phys. Rev. B* **1992**, *45*, 2899–2919.
- (16) Broholm, C.; Cava, R. J.; Kivelson, S. A.; Nocera, D. G.; Norman, M. R.; Senthil, T. Quantum spin liquids. *Science* **2020**, *367*, eaay0668.
- (17) Clair, S.; de Oteyza, D. G. Controlling a Chemical Coupling Reaction on a Surface: Tools and Strategies for On-Surface Synthesis. *Chem. Rev.* **2019**, *119*, 4717–4776.
- (18) Cai, J.; Ruffieux, P.; Jaafar, R.; Bieri, M.; Braun, T.; Blankenburg, S.; Muoth, M.; Seitsonen, A. P.; Saleh, M.; Feng, X.; et al, Atomically Precise Bottom-up Fabrication of Graphene Nanoribbons. *Nature* **2010**, *466*, 470–473.
- (19) Kawai, S.; Nakatsuka, S.; Hatakeyama, T.; Pawlak, R.; Meier, T.; Tracey, J.; Meyer, E.; Foster, A. S. Multiple Heteroatom Substitution to Graphene Nanoribbon. *Sci. Adv.* **2018**, *4*, eaar7181.
- (20) Pawlak, R.; Liu, X.; Ninova, S.; D’Astolfo, P.; Drechsel, C.; Sangtarash, S.; Häner, R.;

- Decurtins, S.; Sadeghi, H.; Lambert, C. J.; et al, Bottom-up Synthesis of Nitrogen-Doped Porous Graphene Nanoribbons. *J. Am. Chem. Soc.* **2020**, *142*, 12568–12573.
- (21) Gross, L.; Mohn, F.; Moll, N.; Liljeroth, P.; Meyer, G. The chemical structure of a molecule resolved by atomic force microscopy. *Science* **2009**, *325*, 1110–1114.
- (22) Song, S.; Su, J.; Telychko, M.; Li, J.; Li, G.; Li, Y.; Su, C.; Wu, J.; Lu, J. On-surface synthesis of graphene nanostructures with π -magnetism. *Chem. Soc. Rev.* **2021**, *50*, 3238–3262.
- (23) Pavliček, N.; Mistry, A.; Majzik, Z.; Moll, N.; Meyer, G.; Fox, D. J.; Gross, L. Synthesis and characterization of triangulene. *Nat. Nanotechnol.* **2017**, *12*, 308–311.
- (24) Turco, E.; Bernhardt, A.; Krane, N.; Valenta, L.; Fasel, R.; Juríček, M.; Ruffieux, P. Observation of the Magnetic Ground State of the Two Smallest Triangular Nanographenes. *JACS Au* **2023**, *3*, 1358–1364.
- (25) Su, J. et al. Atomically precise bottom-up synthesis of π -extended [5]triangulene. *Sci. Adv.* **2019**, *5*, eaav7717.
- (26) Wang, T.; Berdonces-Layunta, A.; Friedrich, N.; Vilas-Varela, M.; Calupitan, J. P.; Pascual, J. I.; Peña, D.; Casanova, D.; Corso, M.; de Oteyza, D. G. Aza-Triangulene: On-Surface Synthesis and Electronic and Magnetic Properties. *J. Am. Chem. Soc.* **2022**, *144*, 4522–4529.
- (27) Vilas-Varela, M. et al. On-Surface Synthesis and Characterization of a High-Spin Aza-[5]-Triangulene. *Angew. Chem. Int. Ed.* **2023**, *62*, e202307884.
- (28) Mishra, S.; Lohr, T. G.; Pignedoli, C. A.; Liu, J.; Berger, R.; Urgel, J. I.; Müllen, K.; Feng, X.; Ruffieux, P.; Fasel, R. Tailoring Bond Topologies in Open-Shell Graphene Nanostructures. *ACS Nano* **2018**, *12*, 11917–11927.

- (29) Mishra, S.; Catarina, G.; Wu, F.; Ortiz, R.; Jacob, D.; Eimre, K.; Ma, J.; Pignedoli, C. A.; Feng, X.; Ruffieux, P.; Fernández-Rossier, J.; Fasel, R. Observation of fractional edge excitations in nanographene spin chains. *Nature* **2021**, *598*, 287–292.
- (30) Wang, T.; Sanz, S.; Castro-Esteban, J.; Lawrence, J.; Berdonces-Layunta, A.; Mohammed, M. S. G.; Vilas-Varela, M.; Corso, M.; Peña, D.; Frederiksen, T.; de Oteyza, D. G. Magnetic Interactions Between Radical Pairs in Chiral Graphene Nanoribbons. *Nano Lett.* **2022**, *22*, 164–171.
- (31) Mishra, S.; Yao, X.; Chen, Q.; Eimre, K.; Gröning, O.; Ortiz, R.; Di Giovannantonio, M.; Sancho-García, J. C.; Fernández-Rossier, J.; Pignedoli, C. A.; Müllen, K.; Ruffieux, P.; Narita, A.; Fasel, R. Large magnetic exchange coupling in rhombus-shaped nanographenes with zigzag periphery. *Nat. Chem.* **2021**, *13*, 581–586.
- (32) Hieulle, J.; Castro, S.; Friedrich, N.; Vegliante, A.; Lara, F. R.; Sanz, S.; Rey, D.; Corso, M.; Frederiksen, T.; Pascual, J. I.; Peña, D. On-Surface Synthesis and Collective Spin Excitations of a Triangulene-Based Nanostar. *Angew. Chem. Int. Ed.* **2021**, *60*, 25224–25229.
- (33) Chen, Z.; Narita, A.; Müllen, K. Graphene Nanoribbons: On-Surface Synthesis and Integration into Electronic Devices. *Adv. Materials* **2020**, *32*, 2001893.
- (34) Rizzo, D. J.; Veber, G.; Jiang, J.; McCurdy, R.; Cao, T.; Bronner, C.; Chen, T.; Louie, S. G.; Fischer, F. R.; Crommie, M. F. Inducing Metallicity in Graphene Nanoribbons Via Zero-Mode Superlattices. *Science* **2020**, *369*, 1597.
- (35) McCurdy, R. D.; Delgado, A.; Jiang, J.; Zhu, J.; Wen, E. C. H.; Blackwell, R. E.; Veber, G. C.; Wang, S.; Louie, S. G.; Fischer, F. R. Engineering Robust Metallic Zero-Mode States in Olympicene Graphene Nanoribbons. *J. Am. Chem. Soc.* **2023**, *145*, 15162–15170.

- (36) Daugherty, M. C.; Jacobse, P. H.; Jiang, J.; Jornet-Somoza, J.; Dorit, R.; Wang, Z.; Lu, J.; McCurdy, R.; Tang, W.; Rubio, A.; Louie, S. G.; Crommie, M. F.; Fischer, F. R. Regioselective On-Surface Synthesis of [3]Triangulene Graphene Nanoribbons. *J. Am. Chem. Soc.* **2024**, *146*, 15879–15886.
- (37) Lawrence, J. et al. Circumventing the stability problems of graphene nanoribbon zigzag edges. *Nat. Chem.* **2022**, *14*, 1451–1458.
- (38) Hapala, P.; Kichin, G.; Wagner, C.; Tautz, F. S.; Temirov, R.; Jelínek, P. Mechanism of High-Resolution STM/AFM Imaging With Functionalized Tips. *Phys. Rev. B* **2014**, *90*, 085421.
- (39) Mohn, F.; Gross, L.; Moll, N.; Meyer, G. Imaging the charge distribution within a single molecule. *Nat. Nanotechnol.* **2012**, *7*, 227–231.
- (40) Meier, T.; Pawlak, R.; Kawai, S.; Geng, Y.; Liu, X.; Decurtins, S.; Hapala, P.; Baratoff, A.; Liu, S.-X.; Jelínek, P.; Meyer, E.; Glatzel, T. Donor–Acceptor Properties of a Single-Molecule Altered by On-Surface Complex Formation. *ACS Nano* **2017**, *11*, 8413–8420.
- (41) Pawlak, R.; Sadeghi, A.; Jöhr, R.; Hinaut, A.; Meier, T.; Kawai, S.; Zajac, L.; Olzowski, P.; Godlewski, S.; Such, B.; Glatzel, T.; Goedecker, S.; Szymoński, M.; Meyer, E. Hydroxyl-Induced Partial Charge States of Single Porphyrins on Titania Rutile. *J. Phys. Chem. C* **2017**, *121*, 3607–3614.
- (42) Turco, E.; Aapro, M.; Ganguli, S. C.; Krane, N.; Drost, R.; Sobrino, N.; Bernhardt, A.; Juríček, M.; Fasel, R.; Ruffieux, P.; Liljeroth, P.; Jacob, D. Demonstrating Kondo behavior by temperature-dependent scanning tunneling spectroscopy. *Phys. Rev. Research* **2024**, *6*, L022061.
- (43) Mishra, S.; Beyer, D.; Eimre, K.; Ortiz, R.; Fernández-Rossier, J.; Berger, R.;

- Gröning, O.; Pignedoli, C. A.; Fasel, R.; Feng, X., et al. Collective all-carbon magnetism in triangulene dimers. *Angewandte Chemie* **2020**, *132*, 12139–12145.
- (44) Anindya, K. N.; Rochefort, A. Spin-polarized topological phases in graphene nanoribbons with non-Benzenoid defects. *The Journal of Physical Chemistry C* **2023**, *127*, 22856–22864.
- (45) Ovchinnikov, A. A. Multiplicity of the ground state of large alternant organic molecules with conjugated bonds: (Do Organic Ferromagnetics Exist?). *Theoretica chimica acta* **1978**, *47*, 297–304.
- (46) Giessibl, F. J. The qPlus sensor, a powerful core for the atomic force microscope. *Rev. Sci. Instrum.* **2019**, *90*, 011101.
- (47) Pawlak, R.; Kawai, S.; Frey, S.; Glatzel, T.; Meyer, E. Atomic-Scale Mechanical Properties of Orientated C₆₀ Molecules Revealed by Noncontact Atomic Force Microscopy. *ACS Nano* **2011**, *5*, 6349–6354.
- (48) Bartels, L.; Meyer, G.; Rieder, K.-H.; Velic, D.; Knoesel, E.; Hotzel, A.; Wolf, M.; Ertl, G. Dynamics of electron-induced manipulation of individual CO molecules on Cu (111). *Phys. Rev. Lett.* **1998**, *80*, 2004.
- (49) Giannozzi, P. et al. QUANTUM ESPRESSO: a modular and open-source software project for quantum simulations of materials. *Journal of physics: Condensed matter* **2009**, *21*, 395502.
- (50) Giannozzi, P. et al. Advanced capabilities for materials modelling with Quantum ESPRESSO. *Journal of Physics: Condensed Matter* **2017**, *29*, 465901.
- (51) Perdew, J. P.; Burke, K.; Ernzerhof, M. Generalized Gradient Approximation Made Simple. *Phys. Rev. Lett.* **1996**, *77*, 3865–3868.

- (52) Rochefort, A.; Anindya, K. N.; Bouju, X.; Denawi, A. H. Magnetic Signature in Graphene Using Adsorbed Metal–Organic Networks. *The Journal of Physical Chemistry C* **2024**, *128*, 919–926.
- (53) Cococcioni, M.; De Gironcoli, S. Linear response approach to the calculation of the effective interaction parameters in the LDA+ U method. *Physical Review B—Condensed Matter and Materials Physics* **2005**, *71*, 035105.
- (54) Grimme, S. Semiempirical GGA-type density functional constructed with a long-range dispersion correction. *Journal of computational chemistry* **2006**, *27*, 1787–1799.
- (55) Blöchl, P. E. Projector Augmented-Wave Method. *Phys. Rev. B* **1994**, *50*, 17953–17979.
- (56) Kresse, G.; Joubert, D. From ultrasoft pseudopotentials to the projector augmented-wave method. *Phys. Rev. B* **1999**, *59*, 1758–1775.

Author contributions

K.N.A., A.R., F.C., R.P. and E.M. conceived the experiments. F.C. synthesized the monomer. R.P. performed STM/AFM measurements with experimental supports from A.H., F.P, O.C, J.-C.L. and C.L. K.N.A. and A.R. performed DFT calculations. R.P., F.C., K.N.A. and A.R. analyzed the data. R.P. wrote the manuscript. All authors discussed on the results and revised the manuscript.

Competing interests

The authors declare no competing financial interests.

Supporting Information Available

Full characterization data for all new compounds.

TOC Graphic